



Originally published as:

Martinez Garzon, P., Kwiatek, G., Bohnhoff, M., Dresen, G. (2017): Volumetric components in the earthquake source related to fluid injection and stress state. - *Geophysical Research Letters*, 44, 2, pp. 800—809.

DOI: <http://doi.org/10.1002/2016GL071963>



## RESEARCH LETTER

10.1002/2016GL071963

## Key Points:

- We calculate and refine 869 full moment tensors of small fluid-induced seismicity from The Geysers geothermal field
- Source types depend on the faulting style and magnitude, suggesting that the stress state has an influence on the volumetric components
- Positive volumetric components increase during high injection periods and near the wells, indicating their relation with pore pressure buildup

## Supporting Information:

- Supporting Information S1
- Data Set S1

## Correspondence to:

P. Martínez-Garzón,  
patricia@gfz-potsdam.de

## Citation:

Martínez-Garzón, P., G. Kwiątek, M. Bohnhoff, and G. Dresen (2017), Volumetric components in the earthquake source related to fluid injection and stress state, *Geophys. Res. Lett.*, *44*, 800–809, doi:10.1002/2016GL071963.

Received 14 NOV 2016

Accepted 12 JAN 2017

Accepted article online 13 JAN 2017

Published online 27 JAN 2017

## Volumetric components in the earthquake source related to fluid injection and stress state

Patricia Martínez-Garzón<sup>1</sup> , Grzegorz Kwiątek<sup>1</sup> , Marco Bohnhoff<sup>1,2</sup> , and Georg Dresen<sup>1,3</sup>

<sup>1</sup>GFZ German Research Centre for Geosciences, Geomechanics and Rheology, Helmholtz Centre Potsdam, Potsdam, Germany, <sup>2</sup>Institute of Geological Sciences, Free University Berlin, Berlin, Germany, <sup>3</sup>Institute of Earth and Environmental Sciences, University of Potsdam, Potsdam, Germany

**Abstract** We investigate source processes of fluid-induced seismicity from The Geysers geothermal reservoir in California to determine their relation with hydraulic operations and improve the corresponding seismic hazard estimates. Analysis of 869 well-constrained full moment tensors ( $M_w$  0.8–3.5) reveals significant non-double-couple components (>25%) for about 65% of the events. Volumetric deformation is governed by cumulative injection rates with larger non-double-couple components observed near the wells and during high injection periods. Source mechanisms are magnitude dependent and vary significantly between faulting regimes. Normal faulting events ( $M_w < 2$ ) reveal substantial volumetric components indicating dilatancy in contrast to strike-slip events that have a dominant double-couple source. Volumetric components indicating closure of cracks in the source region are mostly found for reverse faulting events with  $M_w > 2.5$ . Our results imply that source processes and magnitudes of fluid-induced seismic events are strongly affected by the hydraulic operations, the reservoir stress state, and the faulting regime.

### 1. Introduction

In the analysis of moment tensors of earthquakes, commonly a double-couple shear source is assumed. In recent years, it became gradually accepted that significant non-double couple (NDC) components may contribute to deformation in the earthquake source region [Frohlich, 1994]. Possible physical mechanisms promoting NDC components include fracture opening and closing, mineralogical phase transitions within the seismogenic crust, rupture of nonplanar fault surfaces, or source complexities such as earthquakes composed of more than one subevent. Unfortunately, NDC components are in many cases hard to resolve due to insufficient network geometry or small signal-to-noise ratios. Calculating full moment tensors (FMTs) requires rigorous processing and quality checking, since inaccurate velocity models, crustal anisotropy, or poor coverage of the focal sphere may lead to large artificial NDC components [Julian et al., 1998; Miller et al., 1998; Vavryčuk et al., 2008].

The seismic moment tensor  $\mathbf{M}_{ij}$  may be decomposed using different schemes, including a decomposition into isotropic (ISO), compensated linear vector dipole (CLVD), and double-couple (DC) components [Knopoff and Randall, 1970]. The DC represents the pure shear motion from two orthogonal vector pairs of equal magnitude but opposite sign. The ISO represents the isotropic volumetric change in the earthquake source, with positive values representing tensile opening or explosions, and negative values representing crack closures or implosions. The CLVD represents motion away (if positive) or toward (if negative) the earthquake source with no net volume change and complex physical interpretation [Frohlich, 1994; Julian et al., 1998]. The NDC constitutes the sum of absolute ISO and CLVD components ( $\%NDC = |\%ISO| + |\%CLVD|$ ) and  $|\%ISO| + |\%CLVD| + \%DC = 100\%$ .

In tectonic environments, tensile openings have been detected in pull-apart basins [Stierle et al., 2014] and in earthquake swarms related to natural CO<sub>2</sub> degassing [Vavryčuk, 2002]. Typically, CLVDs are observed in volcanic environments in relation with the collapse of the volcano caldera [Miller et al., 1998; Dreger et al., 2000; Templeton and Dreger, 2006]. Seismic events in mines are often found to contain NDC components associated to rock bursts or the collapse of pillars [Gibowicz, 1989; Šílený and Milev, 2006]. In the last decade, stimulation of unconventional hydrocarbon reservoirs, geothermal systems, and wastewater injection have resulted in a dramatic increase of fluid-induced seismicity [Zoback and Gorelick, 2012; Ellsworth, 2013; McGarr et al., 2015]. Recently, FMT analysis of induced seismic events revealed significant NDC components likely related to the opening of fracture networks, enhancement of permeability, and activation of preexisting critically stressed faults [Cuenot et al., 2006; Fischer and Guest, 2011].

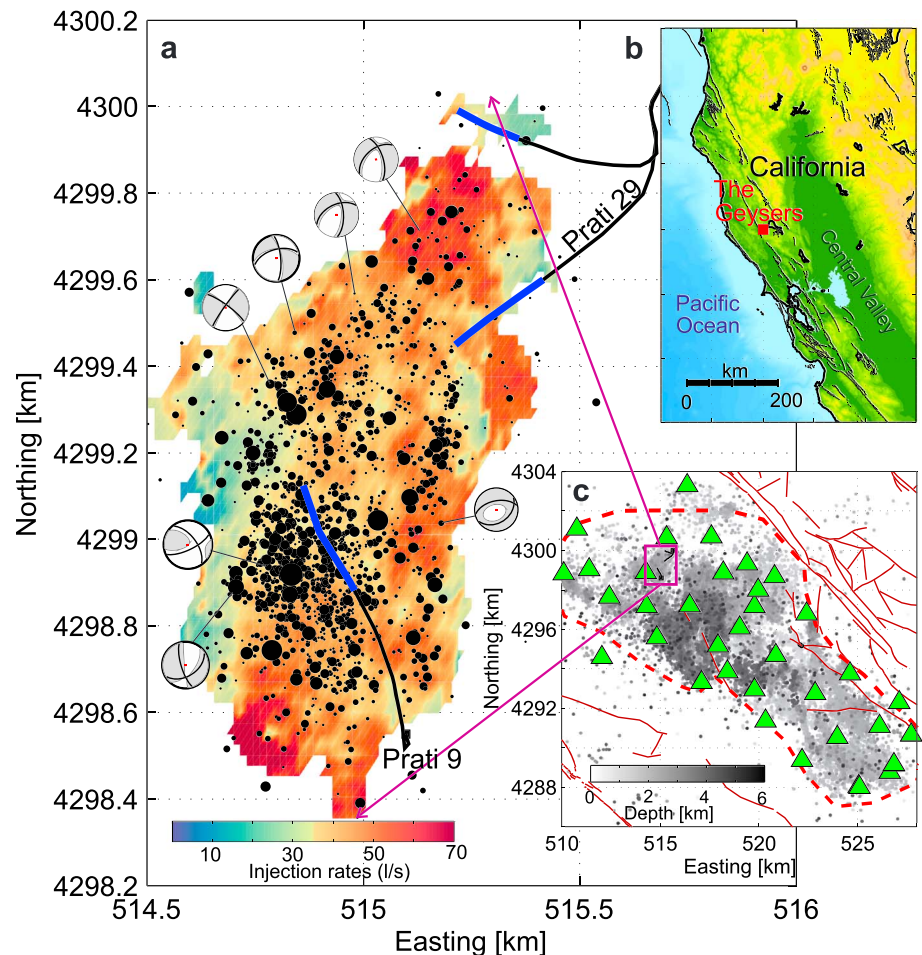


**Figure 1.** (a) Spatial distribution of earthquakes at the northwestern The Geysers geothermal field (black dots). Symbol size is shown encoded with earthquake magnitude, and background color shows smoothed average injection rates at the time of occurrence of the events around that part. Black lines represent the two injection wells nearby, and the blue parts show their open-hole section. The beach balls illustrate selected full moment tensors. (b) Location map of The Geysers geothermal field. (c) Seismicity catalog (dots) and seismic stations (green triangles) throughout the geothermal field. Gray shading represents the hypocentral depth of the events. Dashed red lines represent the reservoir boundaries. Purple rectangle outlines the location of the here analyzed area.

The Geysers geothermal field in Northern California is the largest producing geothermal field in the world. It has been active for more than five decades and has produced several hundreds of thousands of induced seismic events that were monitored by a dense local seismic network. Therefore, it represents an ideal case study to address the potential occurrence of NDC components. At The Geysers, FMTs have been investigated using selected data sets containing between 15 and 30 events, but no clear relation between NDC and fluid injection was found [Ross *et al.*, 1996, 1999; Guilhem *et al.*, 2014; Johnson, 2014]. An additional analysis of 53 events concluded that FMTs from The Geysers-induced earthquakes are complex containing large volumetric components compared to natural seismicity throughout northern California [Boyd *et al.*, 2015].

In this study, we report on a systematic relation between NDC components of induced seismicity and fluid injection rates as well as local stress state. We select a seismicity cluster from the northwestern part of The Geysers and manually revise a high-quality catalog of FMTs composed of 869 small induced earthquakes with moment magnitude ( $M_w$ ) ranging between 0.8 and 3.5. The selected seismicity is constrained within an area of  $\approx 1 \times 2 \text{ km}^2$  and can be directly related to fluid injection into two nearby wells (Figure 1). During the entire 6 year period considered here, the seismicity rates follow closely the water injection volumes [Martínez-Garzón *et al.*, 2013, 2016a, 2016b]. For the first time, our findings allow to relate the resolved NDC components of microseismic events with the hydraulic operations of the two wells as well as the local stress state.

## 2. Method

Many moment tensor inversion techniques rely on fitting synthetic seismograms to the waveform recordings of specified wave trains [e.g., *Sokos and Zahradnik, 2008; Dreger, 2015*]. However, fitting synthetic waveforms is problematic for  $M < \approx 2$  due to e.g. limited data availability, noise, or increased influence of attenuation. *Guilhem et al. [2014]* compared different moment tensor inversions and concluded that  $P$ -wave amplitudes can be successfully inverted to analyze FMTs of small-magnitude events.

Here we employ a hybrid moment tensor inversion [*Kwiatek et al., 2016*] to determine the source processes of the events using manually revised  $P$ -wave amplitudes and allowing for an iterative refinement of FMTs by removing earthquake path effects. We manually picked  $P$ -wave onsets and maximum amplitudes of the  $P$ -wave first motions on the vertical components of ground displacement seismograms of the 32 local stations at The Geysers (Figure 1). A Butterworth second-order high-pass filter at 1 Hz was applied to the waveforms. Takeoff angles were calculated using a local 1-D velocity model [*Eberhart-Phillips and Oppenheimer, 1984*]. For hypocentral depths between 2 and 3 km (representing the vast majority of hypocentral depths used here), the direct wave is faster than the refracted wave for event-station distances smaller than 8–10 km. Accordingly, 69% of the used rays correspond to direct phases. FMTs were estimated and then refined using the hybridMT software [*Kwiatek et al., 2016*], which uses integrals of ground displacement from first  $P$  wave pulses together with sign information as an input for FMT inversion. The refinement of FMT data [*Andersen, 2001*] can be achieved if the distance between the events (here being  $\sim 1.5$  km maximum) is smaller than the distance between events and stations (here having an average of  $\sim 8$  km with respect to local stations). The hybridMT algorithm accounts for poorly known integrated path, site, and/or sensor effects in an iterative procedure. In each iteration, the observed and synthetic amplitudes for each station are compared and the corrections to the Green's functions of each cluster-sensor path are applied. The procedure allowed to identify and adjust for an incorrect gain at station "FNF," which was 6 times lower than expected. The polarity matching between the retrieved moment tensors and the input data reaches  $\sim 90\%$  for the used stations (Figure S1 in the supporting information). All FMTs were visually revised, and those displaying the largest polarity mismatch are eliminated, leaving 869 FMTs for further analysis. Moment tensors, waveforms, and the spectral level (area below the first pulse) for the events with the smallest and largest error are presented in Text S2 and Figure S4.

To evaluate the uncertainty of the retrieved NDC components, we compute for each event synthetic series of 200 FMTs using randomly perturbed input data. For each perturbed input data set, we randomly modify (i) the  $P$ -wave amplitudes up to 10% (simulating site effects [*Davi et al., 2013*]) and (ii) the takeoff angles up to  $\pm 5^\circ$  (simulating uncertainties in the velocity model). This takeoff angle variation represents the standard deviation of 77% of the total amount of phases used for the analysis. It considers the hypocentral event uncertainties and perturbations in the velocity model of up to 10%. The median of the standard deviations of the takeoff angle across the synthetic series is  $1.1^\circ$ .

The calculated source parameters for each event including  $M_w$ , ISO, CLVD, DC,  $P$ ,  $T$ , and  $B$  axes are taken as a mean value derived from the 200 synthetic series. The uncertainties are calculated as two standard deviations from the 200 FMT solutions (95% confidence interval).

We additionally estimate the tensile angle  $\alpha$  from the shear-tensile source model [*Vavryčuk, 2001*] defined as

$$\alpha^{\text{ISO}} = \text{sign}(\% \text{ISO}) \arcsin \frac{|\% \text{ISO}|}{\left(\kappa + \frac{2}{3}\right)(100\% - |\% \text{ISO}|) - \frac{1}{3}|\% \text{ISO}|} \quad (1)$$

as well as the parameter  $\kappa$  being defined as

$$\kappa = \frac{4}{3} \left( \frac{\% \text{CLVD}}{\% \text{CLVD}} - \frac{1}{2} \right) = \frac{\lambda}{\mu}, \quad (2)$$

where  $\lambda$  and  $\mu$  are Lamé's constants.

## 3. Results

Significant NDC components  $|\% \text{ISO}| + |\% \text{CLVD}| > 25\%$  are found in 65% of the 869 analyzed moment tensors, indicating the relevance of considering FMTs to characterize the deformation processes. Out of these events,

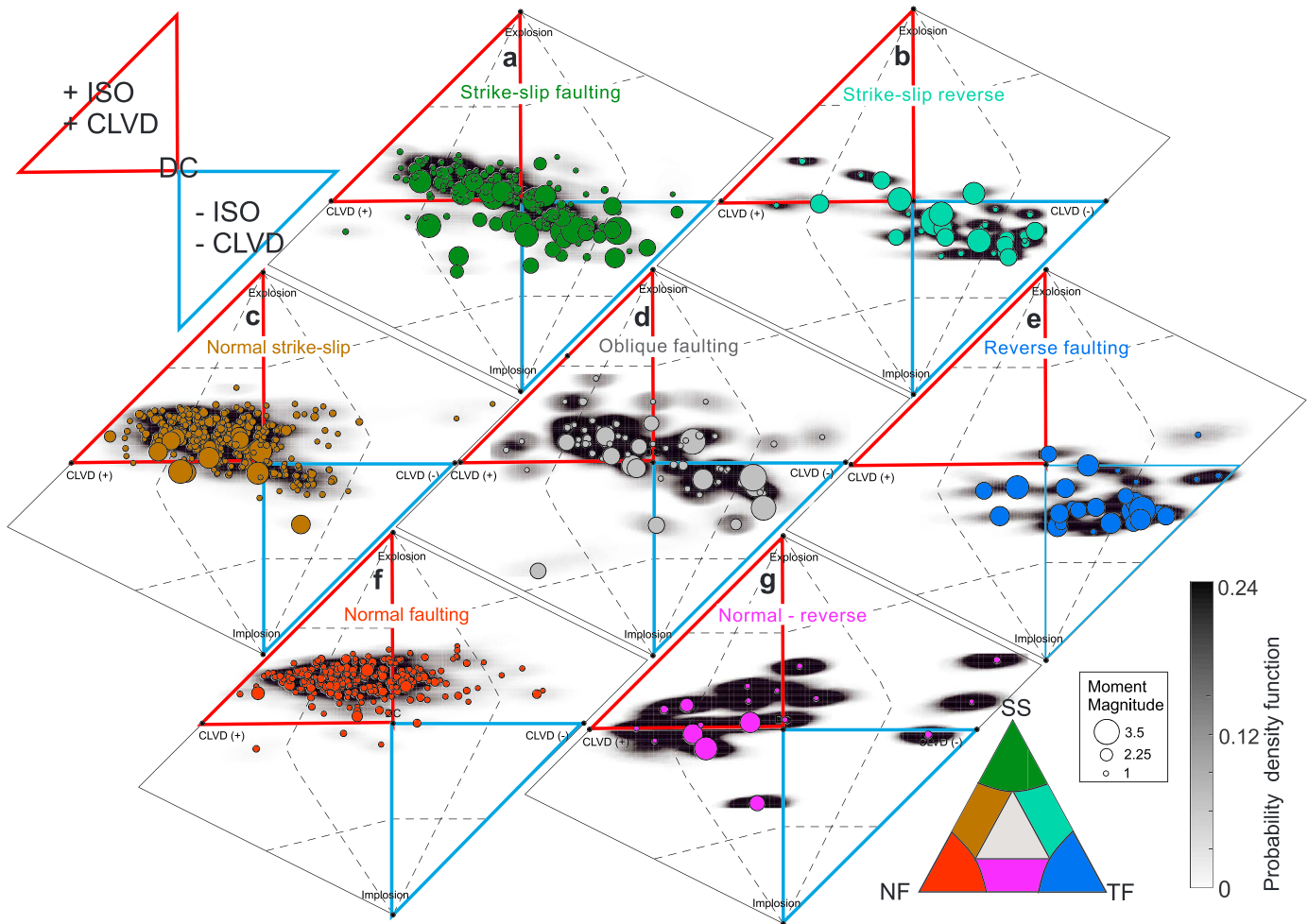


**Figure 2.** Source type plots [Hudson et al., 1989] showing the NDC characteristics of the seismicity separated according to their faulting kinematics. The event kinematics are classified into seven groups according to their corresponding position in the ternary diagram [Frohlich, 1991; 2001]. Symbol size represents the magnitude. Shaded gray color map represents the probability density function of the events representing the 95% confidence interval of the FMT solutions. (a) Strike-slip faulting, (b) strike-slip-reverse faulting, (c) normal-strike-slip faulting, (d) oblique faulting, (e) reverse faulting, (f) normal faulting, and (g) normal-reverse faulting.

about 68% of the FMTs contain positive ISO and CLVD indicating tensile openings or explosions, while about 15% of them display negative ISO and CLVD representing crack closure or implosions.

The data set is divided into three groups with magnitude ranges  $M_w < 1.5$ ,  $1.5 < M_w < 2.5$ , and  $M_w > 2.5$  to estimate the overall uncertainties related to events covering different magnitudes (Figure S2). The median of the uncertainties (95% confidence interval) of the events with  $M_w < 1.5$  and  $1.5 < M_w < 2.5$  are about  $\pm 2\%$ ,  $\pm 5.5\%$ , and  $\pm 6\%$  for the ISO, CLVD, and NDC, respectively. For earthquakes with  $M_w > 2.5$ , the ISO uncertainty remains the same, but the CLVD and NDC uncertainties are larger by  $\approx 1\%$ . Further quality checking is provided in Text S1 and Figures S1–S3.

### 3.1. Source Types in Relation to Faulting Regimes and Seismic Magnitudes

The earthquakes display a wide range of faulting mechanisms including the three Andersonian faulting styles [Anderson, 1951] (normal, strike slip, and reverse). A large diversity in the focal mechanisms was suggested in previous studies based on constrained DC solutions [Martínez-Garzón et al., 2014; Kwiątek et al., 2015]. These results were interpreted to indicate substantial local variations in the stress state, either due to fluid injection operations at the wells nearby or related to structural fault bends within the reservoir rock.

We classify earthquakes according to their faulting kinematics using a ternary fault mechanism diagram [Frohlich, 1991; 2001] (Figure 2). Here the events are separated into three groups corresponding to pure

normal, strike-slip, and reverse faulting and four groups representing mixed mode oblique faulting regimes. We use the respective orientation of the pressure ( $P$ ), tension ( $T$ ), and null ( $B$ ) axes from the FMTs to attribute the events to a regime displayed in the diagram.

Separate source type plots [Hudson *et al.*, 1989] of the FMTs of events belonging to different faulting styles show that seismic events with similar focal mechanisms form distinct clusters with rather similar patterns of NDC components (Figure 2): In general, the source types of strike-slip events are consistent with a DC mechanism with moment tensors displaying both small positive and negative ISO and CLVD components (Figure 2a). In contrast, most of the normal faulting events display significant positive ISO and CLVD representing tensile openings (Figure 2f), and the majority of the reverse faulting events show significant negative ISO and CLVD representing compaction of pore space or crack closure (Figure 2e). Oblique faulting regimes tend to display mixed source types in contrast to pure Andersonian faulting (Figures 2b–2d and 2g). Only 18 events are attributed to a category representing normal-reverse faulting, which would imply a mechanical paradox (Figure 2g). Also, only a limited number of events (mainly normal faulting and strike slip) show FMTs with positive ISO and negative CLVD or vice versa (Figures 2c and 2f). Within the reported confidence intervals for these events the sign of the CLVD components may not be sufficiently constrained. In the following, we only analyze 696 moment tensors with equal sign of ISO and CLVD components.

To investigate a potential relation between event magnitude and source type, the data are sorted with  $M_w$ . Median values of %ISO and %CLVD are calculated in moving magnitude windows containing 20 events and plotted with  $M_w$  (Figures 3a and 3b). We also calculate the tensile angle  $\alpha$  [Vavryčuk, 2001] between slip vector and its projection on the fault plane and present its median from all moment tensors as a function of  $M_w$  (Figure 3c). The median ISO, CLVD, and  $\alpha$  values for a given magnitude range display very similar trends: For earthquake magnitudes between  $0.9 < M_w < 1.6$ , positive median values of ISO  $\approx 16\%$ , CLVD  $\approx 13\%$ , and tensile angle  $\alpha \approx 13^\circ$  are observed, reflecting the tensile opening of fractures. For larger magnitudes  $2 < M_w < 2.5$ , these values become ISO  $\approx 3\%$ , CLVD  $\approx 6\%$ , and tensile angle  $\alpha \approx 6^\circ$ , indicating a decrease in the NDC components and an evolution toward a DC source. For magnitudes of about  $M_w$  2.5–2.6, the FMTs mainly suggest a DC source mechanism. Finally, for magnitudes up to  $M_w = 3$ , the median NDC components become negative, with ISO =  $-10\%$ , CLVD =  $-6\%$ , and  $\alpha \approx -7^\circ$  indicating closure of pore space and fractures in the source region of larger earthquakes (Figure 3).

### 3.2. NDC Components and Fluid Injection Activities

We further analyze the spatiotemporal evolution of the NDC components to evaluate their potential relation with the fluid injection rates in the two nearby wells. Between 2008 and 2014, the well Prati-9 was used to inject waste water into the geothermal reservoir. In addition, a second injection well, Prati-29, started injection in March 2010 lasting to June 2013. The hypocenter seismicity catalog was previously relocated using a double-difference technique [Waldhauser and Ellsworth, 2000], and the volume of the seismicity cloud was observed to vary according to the corresponding injection rates in these wells [Kwiatek *et al.*, 2015] (Figure 1). Here FMTs of events with positive ISO and CLVD are analyzed separately from those with negative ISO and CLVD components, since they may be related to different source processes. Median values of %ISO and %CLVD are calculated taking moving time windows containing 20 events. Finally, we calculate the cumulative injection rates from both wells Prati-9 and Prati-29 for the same moving time windows as above.

The average positive %ISO shows a steady long-term increase from 16% at around 2008 up to 24% toward the end of 2012 (Figure 4a). Concurrently, a long-term decrease in the average positive %CLVD is observed from 23% to 7%. This indicates a long-term increase of positive volumetric changes with injection-induced seismic deformation in the reservoir. Likely, repeated fluid injection also increased the reservoir permeability after several years. The annual injection rates from these wells follow seasonal cycles with larger volumes injected in winter than in summer. Similarly, the temporal evolution of %ISO generally follows the injection rates, with larger values occurring during periods of increased injection volumes. For the %CLVD, a correlation with fluid injection is less clear. Consequently, the ratio  $\kappa$  displays increased values during high injection rates, highlighting the relative increase in the %ISO with respect to the %CLVD at those times.

Seismicity with positive ISO components is more prominent near the injection points at  $<200$  m epicentral distance or at  $<400$  m hypocentral distance (Figure 4b). The discrepancy between the two measures may be due to the  $\approx 200$  m shift between the open-hole section of the Prati-9 well and the center of the seismicity

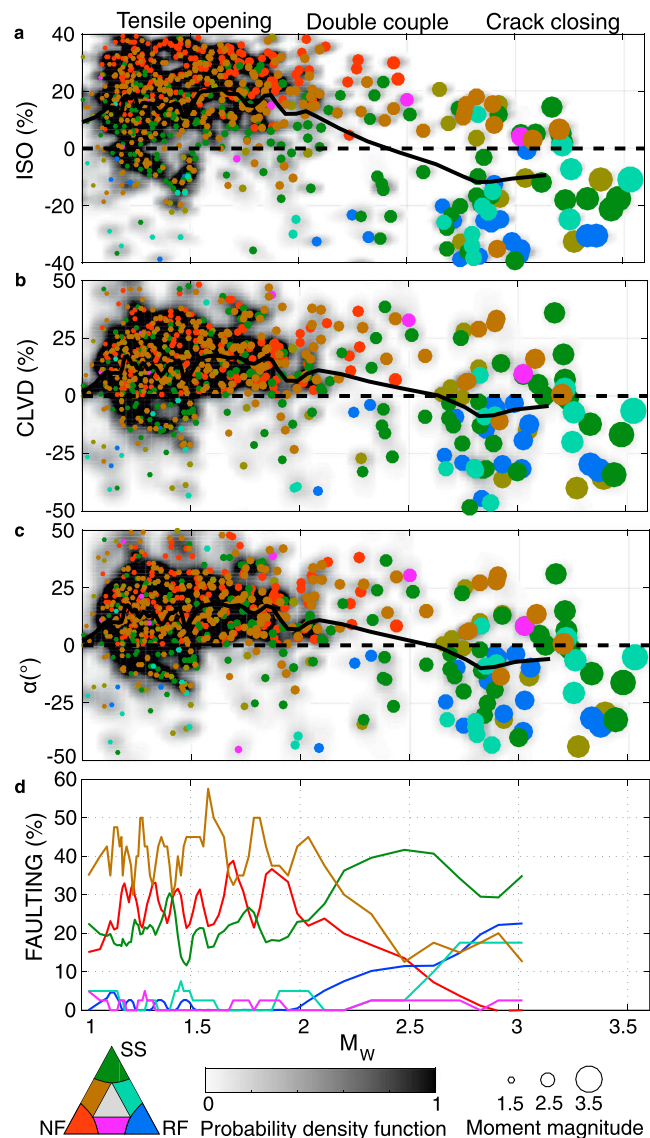


**Figure 3.** Percentages of (a) ISO, (b) CLVD, and (c) tensile angle  $\alpha$  as a function of moment magnitude  $M_w$ . Colored dots display the values for individual FMTs, where the colors represent the faulting kinematics and the symbol size represents the event magnitude. Black line shows the median of the corresponding ISO (Figure 3a), CLVD (Figure 3b), and tensile angle  $\alpha$  (Figure 3c) taking moving magnitude windows containing 20 events. Shaded areas represent the normalized probability density functions reflecting the uncertainty of parameters. (d) Faulting percentage as a function of magnitude for each of the faulting styles according to the ternary diagram.

cloud. We observe a migration of the seismicity with time toward greater depth, coinciding with a general deepening of the seismicity in the reservoir [Kwiatek *et al.*, 2015] (Figure 4c). Interestingly, the positive CLVD components of the seismic events also display a distinct maximum close to the injection wells at or slightly below the open-hole section (<250 m) and decrease with distance (Figure 4b). The observed CLVD maximum around the time of beginning of injection vanished after about 6 month of injection, suggesting that the trend may be somehow related to deformation close to the well during the first injection stages (Figure 4c). The different trends of ISO and CLVD components are reflected by the ratio  $\kappa$  increasing toward larger distances from the wells (Figure 4b).

Fewer moment tensors show negative ISO and CLVD components, and their evolution in space and time is similar to the FMTs with positive NDC (Figure S4). However, the ratio  $\kappa$  is very different for seismicity with positive and negative NDC components: For positive NDC components,  $\kappa > 0.5$  with a mean value

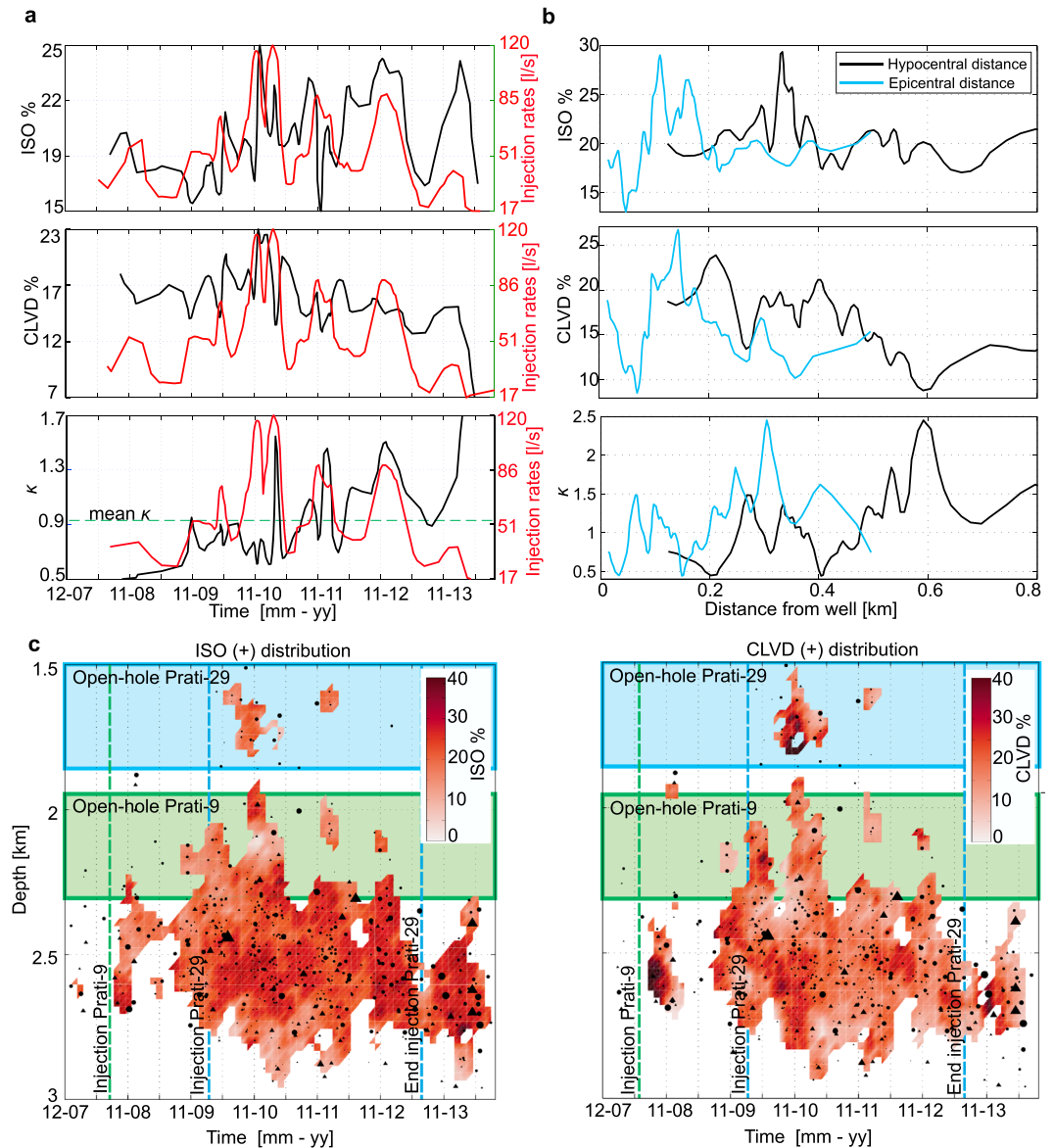


**Figure 4.** (a) Temporal evolution of the positive ISO, CLVD, and  $\kappa$  (black lines) and the averaged aggregated injection rates from the wells nearby (red). (b) Averaged ISO, CLVD, and  $\kappa$  with respect to hypocentral (black) and epicentral (blue) distance from their nearest open-hole section. (c) Depth-time representation of the positive ISO (left) and CLVD (right) components. Individual seismic events are marked with small black symbols. Blue and green rectangles mark the depths of the open-hole sections of the Prati-9 and Prati-29 wells, respectively. Green dashed line indicates injection start at well Prati-9, while dashed blue lines show the start and end of injection at the well Prati-29.

of  $\bar{\kappa} = 0.95$ . For seismicity with negative NDC components,  $\kappa < 0.7$  for most of the analyzed time period and the mean value is  $\bar{\kappa} = 0.5$ . This indicates that the %CLVD is relatively large compared to %ISO for seismic events with negative NDC.

#### 4. Discussion

##### 4.1. The Influence of Stress State on Earthquake Source Types

The analyzed induced earthquakes from The Geysers reveal significant NDC components for most events. Events from the different faulting regimes show distinct characteristic source types. Normal faulting implies extension at relatively lower mean stresses compared to other faulting regimes. This already suggests that tensile NDC components may be favored for seismic events from extensional normal faulting regimes. In



contrast, reverse faulting implies shortening and compaction suggesting that the seismic events contain NDC components indicating crack closure and pore space reduction. Finally, seismicity related to strike-slip faulting is expected to reveal source types centering about DC sources.

We find a correlation of source types with faulting regimes and magnitudes. In addition, we observe that faulting regimes and earthquake magnitudes are also correlated (Figure 3d). About 68% of the  $M_w < 2$  are associated with normal faulting or mixed normal-strike-slip faulting. In contrast, the observed events with largest magnitudes show dominantly reverse faulting and strike-slip mechanisms. The mean and shear stresses required to activate a reverse fault in optimal orientation for failure are larger compared to that of normal and strike-slip faults at similar effective pressures and friction properties. This suggests that the NDC components of seismic events may be strongly affected by the stress state in the source region. Positive NDC components related to tensile opening of cracks are favored at low compressional stresses (i.e., normal faulting). In contrast, for regions subjected to elevated mean effective stress (i.e., reverse faulting), fewer opening fractures would be expected.

In field and laboratory studies, the slope of the earthquake magnitude-frequency distribution (i.e., the  $b$  value) has been found to be inversely proportional to the stress magnitudes with high  $b$  values indicating low stresses and vice versa [Schorlemmer *et al.*, 2005; Goebel *et al.*, 2013; Scholz, 2015]. High  $b$  values characterize a population of events dominated by small magnitudes. Statistical analyses of large seismic data sets have also shown that the  $b$  value is highest in normal faulting regimes compared to reverse faulting, where  $b$  values are lower [Schorlemmer *et al.*, 2005]. This is in very good agreement with our observations. Most of the events with FMTs having positive NDC components have relatively smaller magnitudes and are observed in a normal or transtensional faulting regime. In contrast, lower  $b$  values were reported for seismicity indicating reverse faulting, in good agreement with our observation that reverse faulting events generally show larger magnitudes and dominantly negative NDC components.

In general, this study supports the inference that earthquake magnitude correlates with stress level. We found that the smallest earthquake magnitudes are related to normal faulting at lower differential stresses and that the largest-magnitude events occur with reverse faulting mechanisms likely at elevated differential stresses.

#### 4.2. Implications for the Physical Mechanisms Inducing Seismicity

The FMTs of induced seismic events from our study area show significant NDC components that systematically vary with fluid injection activity. Note that most FMTs of the seismic events indicate dilatation in the source volume and opening of tensile fractures. However, positive and negative NDC components are present and they point towards different concurrent deformation processes occurring in the same region.

Volumetric components (ISO) and the ratio  $\kappa$  increase significantly during time periods of high injection rates, also indicating a strong change of ISO compared to CLVD components. Steam production close to our study area during the considered time periods was negligible compared to the injected volumes. Consequently, we expect the pore pressure in the reservoir to increase around the wells resulting in a pore pressure front that propagates toward larger distances [Martínez-Garzón *et al.*, 2014, 2016b] (Figure 1). We also observe larger ISO and CLVD components of the seismicity immediately surrounding the wells, and the ISO components significantly react to the changes in the injection volumes with time. This suggests that the volumetric (ISO) components of the events depend on the pore pressure level, being larger at relatively higher pore pressures.

Interestingly, the evolution of the CLVD components is also linked to the injection rates, decreasing with distance from the well and also with time after the start of injection (Figure 4b). The interpretation of the observed trends is not straightforward since no physical models are available that allow relating CLVD components uniquely to source mechanics. However, we observed that the distribution of CLVD components in space and time shows a similar trend around the wells as the expected thermal stress changes due to the injection of cold water ( $\approx 30^\circ\text{C}$ ) in the hot reservoir rock (initially  $\approx 240^\circ\text{C}$  [Rutqvist *et al.*, 2013]). Therefore, it is conceivable that enhanced damage close to wells from significant thermal stress changes may promote the occurrence of CLVD components particularly at the beginning of the injection periods. Alternatively, CLVD components may result from two double-couple events at particular fault orientations. Therefore, it is possible that during the initial stimulation period of each well, some of the analyzed microearthquakes may be

composed of more than one subevent from conjugate fault planes. This may result in a composite moment tensor with significant CLVD.

The ratio  $\kappa$  [Vavryčuk, 2001] is related to the seismic  $P$  and  $S$  wave velocities  $V_P$  and  $V_S$ :

$$\kappa = \frac{\lambda}{\mu} = \frac{V_P^2 - 2V_S^2}{V_S^2}. \quad (3)$$

The ratio  $V_P/V_S$  has been used to estimate fluid saturation in The Geysers reservoir [Romero et al., 1995; Julian et al., 1996; Gritto and Jarpe, 2014], and it has been also linked previously to the pore pressure level [Moreno et al., 2014] in subduction zones. In general, at larger fluid saturation  $V_P$  increases and  $V_S$  is reduced resulting in larger  $V_P/V_S$ . At The Geysers, the  $V_P/V_S$  ratio was reported to temporally increase in accordance with a long-term enhancement of injection rates [Gritto and Jarpe, 2014]. Reduced  $V_P/V_S$  ratios in some parts of the reservoir were attributed to elevated steam concentration [Julian et al., 1996]. In the reservoir section analyzed here, larger  $\kappa$  values were observed as fluid injection in this part of the field continued with time. This would agree with larger  $V_P/V_S$  ratios reflecting the accumulation of fluids in this part of the reservoir.

## 5. Conclusions

The analysis of 869 high-quality moment tensors from The Geysers geothermal field allowed to conclude the following main findings:

1. Source types are dependent on the local stress state, with tensile opening identified at lower differential stresses (i.e., normal faulting) and crack closure identified at larger differential stresses (reverse faulting).
2. Faulting style is related with earthquake magnitudes, with normal faulting events displaying an average magnitude  $M_w < 2$ , and larger magnitudes observed for both strike slip and reverse faulting.
3. Volumetric components are more responsive than CLVD components to changes in the injection rates. Larger volumetric components are observed near the injection wells and during time periods of increased injection, suggesting their sensitivity to pore pressure increase.

## Acknowledgments

P.M.G. is grateful to the Helmholtz Association in the frame of the Helmholtz Postdoc Programme for funding. Original hypocentral locations of seismicity were retrieved from the Northern California Earthquake Datacenter (NCEDC). The calculated moment tensors are attached in Table S1. We thank Craig Hartline and the Calpine Corporation Ltd., for providing detailed injection rates for the analyzed wells. We thank the Editor Andrew Newman, Art McGarr, and an anonymous reviewer for their constructive comments that helped to improve the manuscript. We also thank Martin Schoenball for facilitating a programming routine to plot the ternary diagram and Dorina Domigall and Stephan Benz for helping with the preparation of the input data set.

## References

- Andersen, L. M. (2001), *A Relative Moment Tensor Inversion Technique Applied to Seismicity Induced by Mining*, Univ. of the Witwatersrand, Johannesburg, South Africa.
- Anderson, E. M. (1951), *The Dynamics of Faulting and Dyke Formation With Applications to Britain*, Hafner Pub. Co., Houston, Tex.
- Boyd, O. S., D. S. Dreger, V. H. Lai, and R. Gritto (2015), A systematic analysis of seismic moment tensor at The Geysers geothermal field, California, *Bull. Seismol. Soc. Am.*, doi:10.1785/0120140285.
- Cuenot, N., J. Charléty, L. Dorbath, and H. Haessler (2006), Faulting mechanisms and stress regime at the European HDR site of Soultz-sous-Frêts, France, *Deep EGS Enhanc. Geotherm. Syst. Proj. Soultz-Sous-Fr. Alsace Fr.*, 35(5–6), 561–575, doi:10.1016/j.geothermics.2006.11.007.
- Davi, R., V. Vavryčuk, E.-M. Charalampidou, and G. Kwiatak (2013), Network sensor calibration for retrieving accurate moment tensors of acoustic emissions, *Int. J. Rock Mech. Min. Sci.*, 62, 59–67, doi:10.1016/j.ijrmms.2013.04.004.
- Dreger, D. (2015), Earthquake mechanism description and inversion, in *Encyclopedia of Earthquake Engineering*, edited by M. Beer et al., pp. 1–13, Springer, Berlin Heidelberg.
- Dreger, D. S., H. Tkalcic, and M. Johnston (2000), Dilational processes accompanying earthquakes in the Long Valley Caldera, *Science*, 288(5463), 4, doi:10.1126/science.288.5463.122.
- Eberhart-Phillips, D., and D. H. Oppenheimer (1984), Induced seismicity in The Geysers geothermal area, California, *J. Geophys. Res.*, 89, 1191–1207, doi:10.1029/JB089iB02p01191.
- Ellsworth, W. L. (2013), Injection-induced earthquakes, *Science*, 341(6142), doi:10.1126/science.1225942.
- Fischer, T., and A. Guest (2011), Shear and tensile earthquakes caused by fluid injection, *Geophys. Res. Lett.*, 38, L05307, doi:10.1029/2010GL045447.
- Frohlich, C. (1991), Display and quantitative assessment of distributions of earthquake focal mechanisms, *Geophys. J. Int.*, 144, 300–308.
- Frohlich, C. (1994), Earthquakes with non-double-couple mechanisms, *Science*, 264(5160), 804–809, doi:10.1126/science.264.5160.804.
- Frohlich, C. (2001), Display and quantitative assessment of distributions of earthquake focal mechanisms, *Geophys. J. Int.*, 144(2), 300–308, doi:10.1046/j.1365-246x.2001.00341.x.
- Gibowicz, S. J. (1989), Source study of the Lubin, Poland, mine tremor of 20 June 1987, *Acta Geophys. Pol.*, 37, 111–132.
- Goebel, T. H. W., D. Schorlemmer, T. W. Becker, G. Dresen, and C. G. Sammis (2013), Acoustic emissions document stress changes over many seismic cycles in stick-slip experiments, *Geophys. Res. Lett.*, 40, 2049–2054, doi:10.1002/grl.50507.
- Gritto, R., and S. P. Jarpe (2014), Temporal variations of  $V_P/V_S$ -ratio at The Geysers geothermal field, USA, *Geothermics*, 1–8, doi:10.1016/j.geothermics.2014.01.012.
- Guilhem, A., L. Hutchings, D. S. Dreger, and L. R. Johnson (2014), Moment tensor inversions of  $M \sim 3$  earthquakes in the Geysers geothermal fields, California, *J. Geophys. Res. Solid Earth*, 119, 2121–2137, doi:10.1002/2013JB010271.
- Hudson, J. A., R. G. Pearce, and R. M. Rogers (1989), Source type plot for inversion of the moment tensor, *J. Geophys. Res.*, 94, 765–774, doi:10.1029/JB094iB01p00765.
- Johnson, L. R. (2014), Source mechanisms of induced earthquakes at The Geysers geothermal reservoir, *Pure Appl. Geophys.*, 171(8), 1641–1668, doi:10.1007/s00024-014-0795-x.

- Julian, B. R., A. Ross, G. R. Foulger, and J. R. Evans (1996), Three-dimensional seismic image of a geothermal reservoir: The Geysers, California, *Geophys. Res. Lett.*, *23*, 685–688, doi:10.1029/95GL03321.
- Julian, B. R., A. D. Miller, and G. R. Foulger (1998), Non-double-couple earthquakes: 1. Theory, *Rev. Geophys.*, *36*, 525–549, doi:10.1029/98RG00716.
- Knopoff, L., and M. J. Randall (1970), The compensated linear-vector dipole. A possible mechanism for deep earthquakes, *J. Geophys. Res.*, *75*, 1957–1963.
- Kwiatek, G., P. Martínez-Garzón, G. Dresen, M. Bohnhoff, H. Sone, and C. Hartline (2015), Effects of long-term fluid injection on induced seismicity parameters and maximum magnitude in northwestern part of The Geysers geothermal field, *J. Geophys. Res. Solid Earth*, *120*, 7085–7101, doi:10.1002/2015JB012362.
- Kwiatek, G., P. Martínez-Garzón, and M. Bohnhoff (2016), HybridMT: A MATLAB/Shell environment package for seismic moment tensor inversion and refinement, *Seismol. Res. Lett.*, doi:10.1785/0220150251.
- Martínez-Garzón, P., M. Bohnhoff, G. Kwiatek, and G. Dresen (2013), Stress tensor changes related to fluid injection at The Geysers geothermal field, California, *Geophys. Res. Lett.*, *40*, 2596–2691, doi:10.1002/grl.50438.
- Martínez-Garzón, P., G. Kwiatek, H. Sone, M. Bohnhoff, G. Dresen, and C. Hartline (2014), Spatiotemporal changes, faulting regimes, and source parameters of induced seismicity: A case study from The Geysers geothermal field, *J. Geophys. Res. Solid Earth*, *119*, 8378–8396, doi:10.1002/2014JB011385.
- Martínez-Garzón, P., G. Kwiatek, M. Bohnhoff, and G. Dresen (2016a), Impact of fluid injection on fracture reactivation at The Geysers geothermal field, *J. Geophys. Res. Solid Earth*, *121*, 7432–7449, doi:10.1002/2016JB013137.
- Martínez-Garzón, P., V. Vavryčuk, G. Kwiatek, and M. Bohnhoff (2016b), Sensitivity of stress inversion of focal mechanisms to pore pressure changes, *Geophys. Res. Lett.*, *43*, 8441–8450, doi:10.1002/2016GL070145.
- McGarr, A., et al. (2015), Coping with earthquakes induced by fluid injection, *Science*, *347*(6224), 830–831, doi:10.1126/science.aaa0494.
- Miller, A. D., G. R. Foulger, and B. R. Julian (1998), Non-double-couple earthquakes: 2. Observations, *Rev. Geophys.*, *36*, 551–568, doi:10.1029/98RG00717.
- Moreno, M., C. Haberland, O. Oncken, A. Rietbrock, S. Angiboust, and O. Heidbach (2014), Locking of the Chile subduction zone controlled by fluid pressure before the 2010 earthquake, *Nat. Geosci.*, *7*(4), 292–296, doi:10.1038/ngeo2102.
- Romero, J., T. V. McEvilly, E. L. Majer, and Vasco (1995), Characterization of the geothermal system beneath the Northwest Geysers steam field, California, from seismicity and velocity patterns, *Geothermics*, *24*(4), 471–487, doi:10.1016/0375-6505(95)00003-9.
- Ross, A., G. R. Foulger, and B. R. Julian (1996), Non-double-couple earthquake mechanisms at the Geysers Geothermal Area, California, *Geophys. Res. Lett.*, *23*, 877–880, doi:10.1029/96GL00590.
- Ross, A., G. R. Foulger, and B. R. Julian (1999), Source processes of industrially-induced earthquakes at The Geysers geothermal area, California, *Geophysics*, *64*(6), 1877–1889, doi:10.1190/1.1444694.
- Rutqvist, J., P. F. Dobson, J. Garcia, C. Hartline, P. Jeanne, C. M. Oldenburg, D. W. Vasco, and M. Walters (2013), The Northwest Geysers EGS demonstration project, California: Pre-stimulation modeling and interpretation of the stimulation, *Math. Geosci.*, *1–27*, doi:10.1007/s11004-013-9493-y.
- Scholz, C. H. (2015), On the stress dependence of the earthquake *b*-value, *Geophys. Res. Lett.*, *42*, 1399–1402, doi:10.1002/2014GL02863.
- Schorlemmer, D., S. Wiemer, and M. Wyss (2005), Variations in earthquake-size distribution across different stress regimes, *Nature*, *437*(7058), 539–542, doi:10.1038/nature04094.
- Šílený, J., and A. Milev (2006), Seismic moment tensor resolution on a local scale: Simulated rockburst and mine-induced seismic events in the Kopanang Gold Mine, South Africa, *Pure Appl. Geophys.*, *163*(8), 1495–1513, doi:10.1007/s00024-006-0089-z.
- Sokos, E. N., and J. Zahradnik (2008), ISOLA—A Fortran code and Matlab GUI to perform multiple point source inversion of seismic data, *Comput. Amp Geosci.*, *34*(8), 967–977, doi:10.1016/j.cageo.2007.07.005.
- Stierle, E., V. Vavryčuk, J. Šílený, and M. Bohnhoff (2014), Resolution of non-double-couple components in the seismic moment tensor using regional networks—I: A synthetic case study, *Geophys. J. Int.*, doi:10.1093/gji/ggt502.
- Templeton, D. C., and D. S. Dreger (2006), Non-double-couple earthquakes in the Long Valley volcanic region, *Bull. Seismol. Soc. Am.*, *96*(1), 69–79, doi:10.1785/0120040206.
- Vavryčuk, M., Z. Bohnhoff, P. K. Jechumtálová, and J. Šílený (2008), Non-double-couple mechanisms of microearthquakes induced during the 2000 injection experiment at the KTB site, Germany: A result of tensile faulting or anisotropy of a rock?, *Tectonophysics*, *456*, 74–93, doi:10.1016/j.tecto.2007.08.019.
- Vavryčuk, V. (2001), Inversion for parameters of tensile earthquakes, *J. Geophys. Res.*, *106*, 16,339–16,355, doi:10.1029/2001JB000372.
- Vavryčuk, V. (2002), Non-double-couple earthquakes of 1997 January in West Bohemia, Czech Republic: Evidence of tensile faulting, *Geophys. J. Int.*, *149*(2), 364–373, doi:10.1046/j.1365-246X.2002.01654.x.
- Waldhauser, F., and W. L. Ellsworth (2000), A double-difference earthquake location algorithm: Method and application to the Northern Hayward Fault, California, *Bull. Seismol. Soc. Am.*, *90*(6), 1353–1368, doi:10.1785/0120000006.
- Zoback, M. D., and S. M. Gorelick (2012), Earthquake triggering and large-scale geologic storage of carbon dioxide, *Proc. Natl. Acad. Sci. U.S.A.*, *109*, 201202473, doi:10.1073/pnas.1202473109.